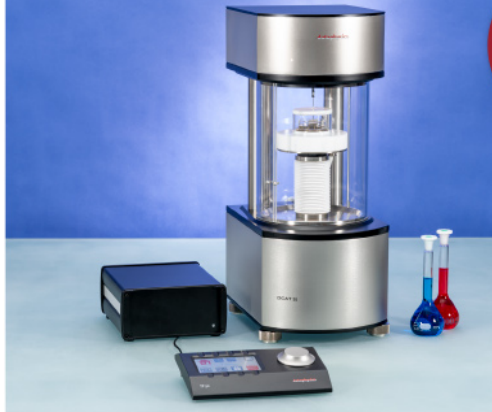




ASTM D5946
ASTM D7334
ASTM D7490
ISO 27448

optische Kontaktwinkel-
messung und Tropfenkon-
turanalyse zur Bestimmung
von Oberflächenenergie
sowie Grenz- und
Oberflächenspannung

kraftbasierte Tensiometrie,
dynamische Kontaktwinkel-
messung und Bestimmung
der Adhäsionskraft



ASTM D1331
ASTM D1417
ISO 1409

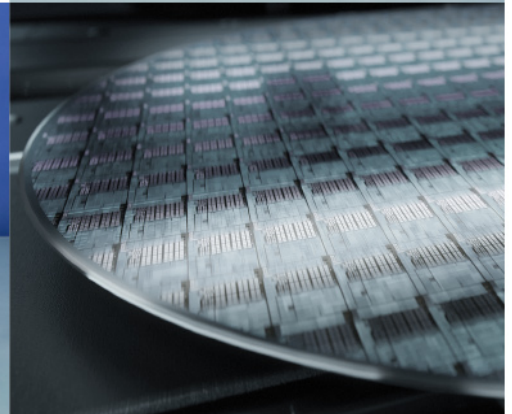


ISO/TR 13097

optische Stabilitäts-
und Alterungsanalyse
mehrfasiger Dispersionen



Zeta-Potential-Messung
auf Fasern, Pulvern
und plattenförmigen
Festkörpern



Vielseitige Laboranalysegeräte für die
umfangreiche Charakterisierung von
Materialoberflächen und der Wechsel-
wirkungen zwischen Werkstoffen.

Mehr erfahren >

dataphysics
Understanding Interfaces

DataPhysics Instruments GmbH
Raiffeisenstraße 34 • 70794 Filderstadt, Deutschland
Telefon +49 (0)711 770556-0 • Fax +49 (0)711 770556-99
sales@dataphysics-instruments.com
www.dataphysics-instruments.com

Investigation of the potential of topology optimization in additive manufacturing using the example of components subject to bending stress

Untersuchung des Potenzials der Topologieoptimierung in der additiven Fertigung am Beispiel von biegebeanspruchten Bauteilen

D.R. Jantos¹ , A. Röttger², P. Junker¹

In this application-oriented work, we examine the performance of topology-optimized structures as compared to the reference I-beam. We make use of the thermodynamic topology optimization based on a linear elastic compliance minimization, i.e. minimization of the elastic strain energy of the whole structure. We investigate, how the optimization of the rather theoretical strain energy influences the efficiency of more practical measurements, i.e. the force-displacement response at the loading points and the maximum tolerable force. For this purpose, starting from a cuboid design space with the boundary conditions of a 3-point and 4-point bending stress, the geometry with constant volume was optimized. The topology-optimized bending beams were subsequently produced by stereolithography and mechanically tested with respect to the previously defined boundary conditions. In order to avoid a falsification of results due to internal sample defects, all samples were previously examined with the aid of computer tomography with regard to the defects in the volume. As a general result, the topology-optimized bending beams can bear a higher load in the experiment, which shows the usefulness of the coupling of additive manufacturing and topology optimization methods without any special constraints or enhancements regarding the manufacturing process within the optimization.

Keywords: Topology optimization / additive manufacturing / stereolithography

Schlüsselwörter: Topologieoptimierung / Additive Fertigung / Stereolithographie

1 Introduction

The efficient use of resources, i.e. energy and production materials, becomes more and more important. For structural engineering, the topology optimization became an important tool over the last decades to reduce material usage and weight of components without sacrificing mechanical per-

formance. Many approaches were developed and can be found in literature. For an overview over topology optimization methods we refer to the review papers [1–3].

Although common topology optimization methods yield distinct optimized geometries, i.e. either full material or absence of material within each point of a given design space, those geometries are

¹ Institute of Continuum Mechanics, Leibniz University Hannover, Germany

² New Manufacturing Technologies and Materials, University of Wuppertal, Germany

Corresponding author: D.R. Jantos, Institute of Continuum Mechanics, Leibniz University Hannover, Germany,
E-Mail: jantos@ikm.uni-hannover.de

often difficult to produce with conventional production techniques like subtractive processes or casting. Within the last years, different additive manufacturing processes were developed and substantially improved. Established techniques are for example laser powder bed fusion (L-PBF), directly energy deposition (DED), stereolithography (SLA), jetting techniques, and fused deposition modeling (FDM). Overviews over the different techniques and their properties can be found in [4–6]. Depending on the additive manufacturing process, metals, ceramics, polymers, or biological tissue can be used for production of solids, so that additive manufacturing becomes interesting for various industrial fields. Besides the material variety, additive manufacturing processes are based on the layer-by-layer production of solid geometries, which allows for an extreme design freedom compared to conventional manufacturing. Especially, the production effort only increases slightly with increased complexity of the geometries, which makes additive manufacturing suitable for the production of topology optimization results possession complex and often fine structures. Works regarding the additive manufacturing of optimized structures and also discussing enhancements of topology optimization methods to accommodate additive manufacturing and vice versa are reviewed in [7–9].

The aim of this work is the fundamental investigation of the performance of topology-optimized structures as compared to reference structures subject to bending by applying a compliance minimization topology optimization with isotropic and linear elastic material and prosumer level additive manufacturing-equipment. The topology optimization in terms of a compliance minimization, i.e. minimizing the strain energy in the whole body, was carried out for a 3-point and 4-point bending boundary value problem. The reference structure was the I-beam. For the topology optimization, we applied the thermodynamic topology optimization [10]. The thermodynamic optimization already proved beneficial for different enhancements regarding anisotropic (fiber) materials and tensile and compression affine materials (steel-concrete) [11, 12]. Nevertheless, most results regarding the thermodynamic optimization were only examined in silico but not produced and tested in situ. Thus, topology-optimized bending beams were subsequently converted into an STL file-format and

samples for mechanical testing were manufactured using stereolithography. Hereby, no constraints or enhancements regarding additive manufacturing are applied within the optimization to examine the performance of basic topology optimization schemes with linear elastic material without stress constraint or failure criterion. Nevertheless, it is examined if the optimization improves the component strength, i.e. the maximum tolerable forces, and the force-displacement response at the loading point.

Tensile tests were set up both vertically and horizontally to the direction of construction in order to illustrate the influence of the direction of construction on the material properties. Internal defects of the test specimens were examined using micro computed tomography. These microtomography examinations provide information about the effect of internal defects on the premature failure of the manufactured specimen under bending stress. With this procedure, the effect of topology optimization can be clearly quantified without the disruptive influence of sample defects.

The method used for topology optimization will be briefly discussed in section 2 below. It is followed by the experimental implementation of the result validation in section 3 and the presentation and discussion of the results in section 4.

2 Thermodynamic topology optimization

2.1 Brief introduction to thermodynamic topology optimization

We used the thermodynamic topology optimization for the compliance minimization under volume (material amount) constraint of an isotropic linear elastic material [10]. For a detailed explanation and derivations, we refer to the original publication.

The thermodynamic optimization is based on the Hamilton principle and reads for a given design space Ω

$$\delta_u \mathcal{G}(\mathbf{u}, \chi) = 0 \quad \forall \delta \mathbf{u} \quad (1)$$

$$\begin{aligned} \delta_\chi \mathcal{G}(\boldsymbol{\sigma}, \chi) + \int_{\Omega} \frac{\partial \mathcal{D}(\dot{\chi})}{\partial \dot{\chi}} \delta \chi \, dV + \delta_\chi \mathcal{C}(\chi) \\ + \delta_\chi \mathcal{R}(\nabla \chi) = 0 \quad \forall \delta \chi \end{aligned} \quad (2)$$

where $\delta_{\mathbf{u}}\mathcal{G}$ and $\delta_{\chi}\mathcal{G}$ describe the Gateaux derivatives, i.e. “total variational derivative”. Those variables and therefore the unknowns of the problems are the displacements $\mathbf{u}(\mathbf{x}) \forall \mathbf{x} \in \Omega$ and the design variable χ which represents the continuous density $\chi(\mathbf{x}) \in [0, 1] \forall \mathbf{x} \in \Omega$ defining the topology with

$$\chi = \begin{cases} 0 & \text{for void} \\ 1 & \text{for full material} \end{cases} \quad (3)$$

The Gibbs energy reads

$$\mathcal{G} = \int_{\Omega} \Psi dV - \int_{\Omega} \mathbf{b} \cdot \mathbf{u} dV - \int_{\partial\Omega} \mathbf{t} \cdot \mathbf{u} dV \quad (4)$$

where $\partial\Omega$ denotes the boundary of the design space. The body forces \mathbf{b} and traction forces \mathbf{t} are given as constant, i.e. they are neither a function of the displacements \mathbf{u} nor the density χ . The variation of the Gibbs energy $\mathcal{G}(\mathbf{u}, \chi)$ with the Helmholtz free energy

$$\Psi(\mathbf{u}, \chi) = \frac{1}{2} \boldsymbol{\varepsilon}(\mathbf{u}) : \mathbf{E}(\chi) : \boldsymbol{\varepsilon}(\mathbf{u}) \quad (5)$$

yields the mechanical equilibrium, i.e. principle of virtual work, with the strain denoted by $\boldsymbol{\varepsilon}$ and the elastic material tensor or material stiffness tensor denoted by \mathbf{E} . The formulation $\mathcal{G}(\boldsymbol{\sigma}, \chi)$ with

$$\Psi(\boldsymbol{\sigma}, \chi) = \frac{1}{2} \boldsymbol{\sigma} : [\mathbf{E}(\chi)]^{-1} : \boldsymbol{\sigma} \quad (6)$$

describes the objective function of the optimization, i.e. compliance minimization, with the stress denoted by $\boldsymbol{\sigma}$. We apply the power-law material interpolation used in solid isotropic material with penalization (SIMP) approaches [13]

$$\mathbf{E}(\chi) = [(1 - \kappa)\chi^3 + \kappa] \mathbf{E}_0 \quad (7)$$

with the manufacturing material \mathbf{E}_0 to penalize and suppress intermediate densities $\chi \in [0, 1]$ from the resulting topology. Herein, $\kappa = 10^{-9}$ is a small but non-zero numerical value to prevent singularities within the finite element method, which is used to

solve the mechanical equilibrium (1) within each optimization step.

The dissipation function $\mathcal{D} = \frac{1}{2} \eta \dot{\chi}^2$ enables the derivation of the so-called evolution equation: a partial differential equation whose (iterative) solution yields the optimal design. Herein, η describes the viscosity, which accounts for numerical damping and has no direct physical meaning. The volume constraint

$$\int_{\Omega} \chi dV = \Omega_S \quad (8)$$

with the prescribed structure volume Ω_S and the interval constraint $\chi \in [0, 1]$ is given by the functional \mathcal{C} . The required Lagrange multiplier λ for the volume constraint and the Karush-Kuhn-Tucker parameters γ for the enforcement of the admissible interval for χ are determined by a bisection algorithm within each iteration step.

The functional $R = \int_{\Omega} \frac{1}{2} \beta^* |\nabla|^2 dV$ with the Nabl-Operator ∇ describes a gradient-enhanced regularization to suppress checkerboarding, grants mesh independent results, controls the minimum member size of the structure, i.e. the minimum radius of trusses within the topology, which is given by the parameter $r_{min} = \sqrt{\beta^*}$ with

$$\beta = \beta^* \frac{\int_{\Omega} \tau_{\chi} (1 - \chi) dV}{\int_{\Omega} \chi (1 - \chi) dV} \quad (9)$$

The variation of the Hamilton principle with respect to the design variable, i.e. the density χ , given in Eq. (2) yields the driving forces (sensitivities)

$$\begin{aligned} \tau_{\chi} &= \frac{1}{2} \boldsymbol{\varepsilon} : \frac{\partial \mathbf{E}}{\partial \chi} : \boldsymbol{\varepsilon} \\ &= \frac{1}{2} \boldsymbol{\varepsilon} : (3(1 - \kappa)\chi^2) \mathbf{E}_0 : \boldsymbol{\varepsilon} \end{aligned} \quad (10)$$

and the evolution equation

$$\dot{\chi} = \frac{1}{2} (\tau_{\chi} - \lambda - \gamma + \beta \nabla \cdot \nabla \chi) \quad \forall \mathbf{x} \in \Omega \quad (11)$$

including the Neumann boundary conditions

$$\nabla \chi \cdot \mathbf{n} = 0 \quad \forall \mathbf{x} \in \partial\Omega \quad (12)$$

The optimal design is determined by an iterative process consisting of an alternating finite element analysis to solve the mechanical equilibrium (1) for the displacements \mathbf{u}^i with a given design χ^i and a design update by evaluating the evolution equation (11) with an explicit time discretization

$$\chi^{i+1} = \chi^i + \Delta t \dot{\chi}(\mathbf{u}^i, \chi^i) \tag{13}$$

wherein the time steps i become the iteration steps of the optimization process and the time increment Δt and viscosity η account for numerical damping. The Laplace-operator $\nabla \cdot \nabla \chi^i$ within the evolution equation is calculated via the method introduced in [10].

2.2 Numerical results and reference geometry

The free design space¹ is enclosed by two base walls, which are not part of the optimization and are predefined as full material with $\chi = 1$, Figures 1, 2. The geometric dimensions are given in (normalized) dimensionless length and volume units. The manufactured specimens are scaled by a factor of 62 mm resulting in an over-all length of 80 mm for the specimen. The supports at the base walls correspond to a solid surface on which the specimen is placed and the forces are applied in a line along the whole width of the free design space, Figure 2 (in view direction).

A (dimensionless) structure volume $\Omega_s = 0.132$ including the base walls and $\Omega_s = 0.05$ without the base walls is prescribed for the topology optimization (about 40 % of the free design space is filled with material). We compare the results of the topology optimization with a reference model given by an I-beam, Figure 3. The beam is also enclosed in base walls and its volume is chosen to be identical to the prescribed structure volume within the topology optimization. Thus, the thickness for the beam cross section area has to be $t = 0.052$.

The minimum member size for the topology optimization is chosen to be $r_{min} = 0.035$. Thus, with the scaling for production of 62 mm, the chosen

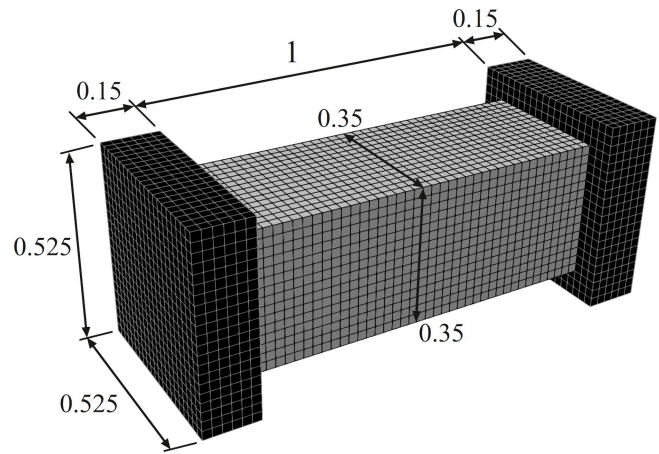


Figure 1. Finite element mesh and dimensions of the design space for the topology optimization.

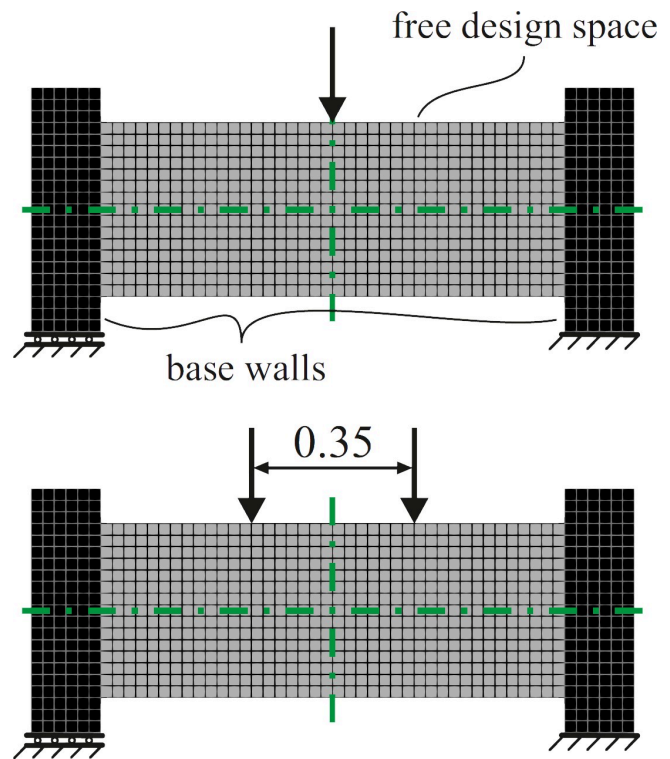


Figure 2. Boundary conditions for the three-point bending and the four-point bending.

minimum member size will yield designs with features not smaller than about 2.17 mm in diameter. Although the stereolithography-printer is capable of printing smaller features, trusses and walls with diameter or thickness less than 2.17 mm are vulnerable to warping or breakage during the post-processing of the print, i.e. during the cleaning in alcohol or while removing the supports.

¹Per definition, the design space Ω includes all structural members and therefore the free design space and the base walls.

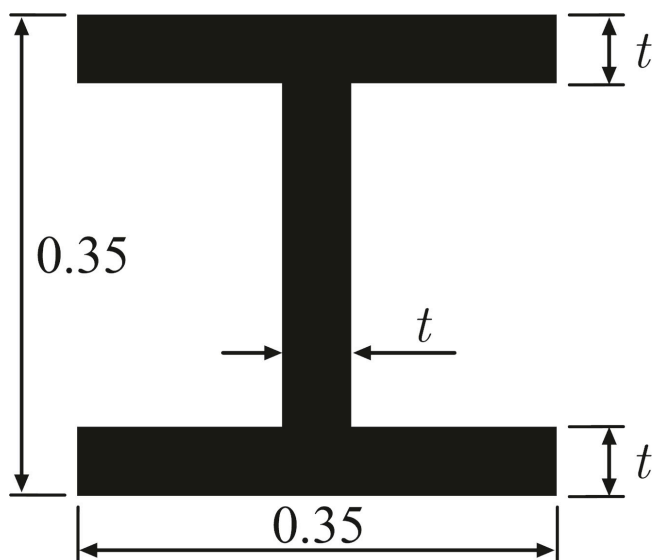


Figure 3. Cross section of the reference I-beam.

The model is discretized by $15 \times 15 \times 40$ finite elements for the free design space and $21 \times 21 \times 6$ finite elements for each base wall. The element-size of the regular mesh is $h = 0.0125$ (dimensionless length), which is smaller than the chosen minimum member size r_{min} so that no numerical instabilities

as checkerboarding or mesh dependence will occur, but the calculation effort is reduced, *Figure 4*. Finer meshes would yield the same results for the topology for the given value of the minimum member size [10]. However, the optimization model is also suitable for finer meshes and structures, i. e. smaller minimum member sizes, although those structures were not produced due to the manufacturing limitations mentioned above, *Figure 5*.

For the linear elastic material, we apply a Poisson's ratio of 0.3, whereas the value of Young's modulus does not influence the resulting topology due to the linear theory and can be chosen arbitrarily.

In a post-processing step, the element-wise discretized density² χ is linearly extrapolated to the nodes of the finite element mesh and the final topology is represented by the (triangulated) iso-surface with a threshold value of 0.5 for the extrapolated density. Thus, 3D-models with smooth surfaces rather than voxel-based representations are generated for the visual representation and the production models for additive manufacturing. The resulting 3D-models are saved as STL-files and can be scaled within the respective slicer software corresponding to the used 3D-printers.

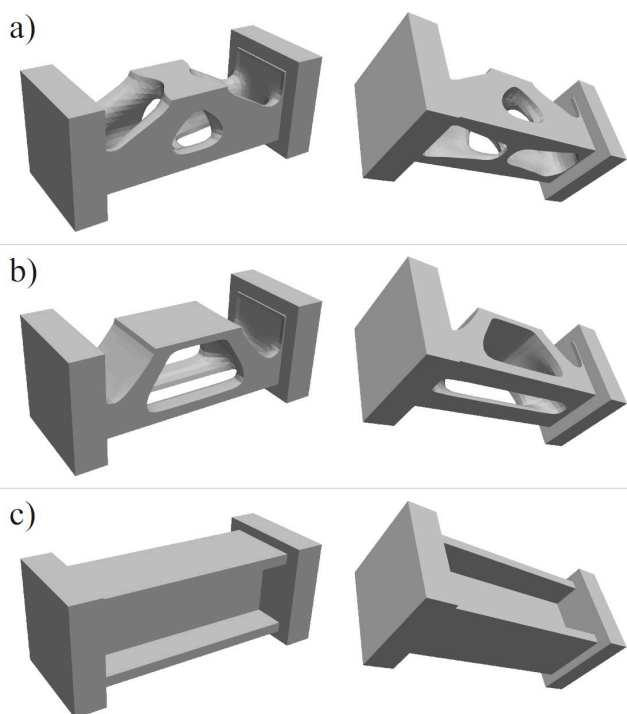


Figure 4. Results of the topology optimization for: a) the three-point bending, b) the four-point bending, and c) the reference I-beam.

3 Experimental investigation

3.1 Materials and sample preparation

In this work, standard photopolymer resins FLGP04 from the company Formlabs were used which only differ in their color. This resin is a photo-polymer that does not require a special post-curing process. Significant properties of the photo-polymer were taken from the manufacturer's instructions and are listed, *Table 1*. Samples were manufactured using the Form2 stereolithography printer from the company Formlabs. The samples were manufactured with a 250 mW diode laser (405 nm) and a layer thickness of $50 \mu\text{m}$ taking into account a z -compression correction of 0.75 mm.

²Used software is *ParaView*. The iso-surface is generated with the *Cell Data to Point Data*, *Iso-Volume*, and *ExtractSurface* filters. The triangulated surface is subsequently saved in the STL-file format for production of specimens with a SLA-printer.

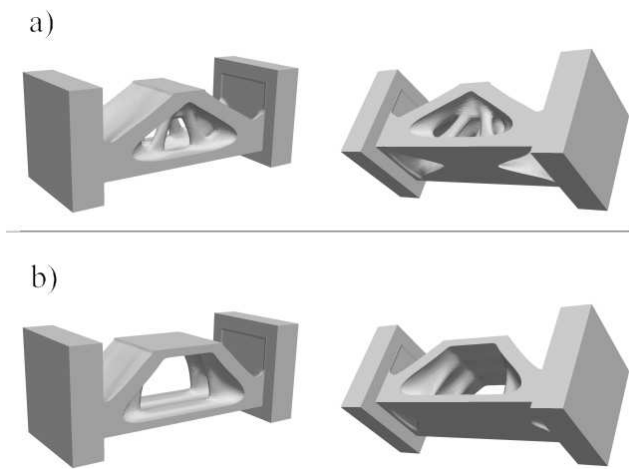


Figure 5. a) the three-point bending, b) the four-point bending. Results of the topology optimization with finer mesh ($30 \times 30 \times 80$ elements for the free design space) and smaller minimum member size $r_{min} = 0.0175$ (about 1 mm for a 80 mm wide specimen). Those models were not produced and tested.

Table 1. Material properties according to the manufacturer Formlabs.

Material properties	Tensile modulus [GPa]	Tensile stress [MPa]	Elongation at break [%]
green	1.6	38	12
post-cured	2.8	65	6.2

The assembly accuracy in the x and y direction is specified by the manufacturer as $25 \mu\text{m}$. The sample production took place with the automatic creation of the support structures using the printer's slicer (software) PreForm 3.0.1. For statistical reasons, five tensile specimens in the vertical and horizontal directions to determine the material properties and eight 3-point, eight 4-point specimens, and eight I-beam structures were fabricated on the same machine (four with clear and four with black resin each). Built specimens were cleaned with a 99% isopropanol alcohol and further hardened for 15 minutes in a light curing device (Technotray Powder, Heraeus Kulzer) with wavelengths of 450 nm to 475 nm at around 60°C .

3.2 Microtomography investigation

Defects in the volume of the stereolithography-manufactured specimens were examined with the

aid of micro computed tomography. The aim of these investigations was to describe the influence of these volume defects on the bearable load, so that the positive influence of the topology optimization can be quantified without the influence of defects. For this purpose, all samples were examined for internal defects using the micro-computer tomography before mechanical testing. EasyTom 160 μCT from RX Solution was used, equipped with a tungsten filament and a tungsten target. The parameters set for the x-ray source were a tube current of $37.4 \mu\text{A}$, a target current of $30 \mu\text{A}$ and a working voltage of 90 kV. The microtomograph is equipped with a flat panel imager detector $238 \text{ mm} \times 190 \text{ mm}$. This detector possesses a resolution of $1920 \text{ pixels} \times 1536 \text{ pixels}$. The maximum resolution of internal defects results from the geometric conditions between the sample size and the minimum distance between the x-ray source, sample and detector. The voxel size resolution of the 3- and 4-point bending samples is about $32 \mu\text{m}$ to $32.5 \mu\text{m}$ and $44 \mu\text{m}$ to $44.5 \mu\text{m}$ for the I-beam structures. For the evaluation of volume images, five images were taken with a gray value resolution of 16 bits (corresponds to 65536 gray levels) per slice, from which an average image was generated. The mean value images were subsequently read into the Xact (RX Solution) program for image construction. The reconstruction was carried out on the basis of the y-slices with an automatic OffsetX correction. The evaluation of defects and the image generation was carried out with the program VG-Studio MAX (volume graphics).

3.3 Mechanical testing

For the determination of selected material properties, tensile tests according to DIN EN 10002 were carried out. For this purpose, the Z100-Roell universal strain-compression test machine Z100 was used. During the tensile test, the force was determined with a 100 kN load cell and the sample extension was gathered by the traverse path. The samples were preloaded with a compression force of 15 N and tested to failure with a crosshead travel speed of 0.5 mm per minute. The 3-point and 4-point bending tests were carried out with the samples based on the standard DIN EN ISO 14125, Figure 6. Contrary to the standard, the sample supports were

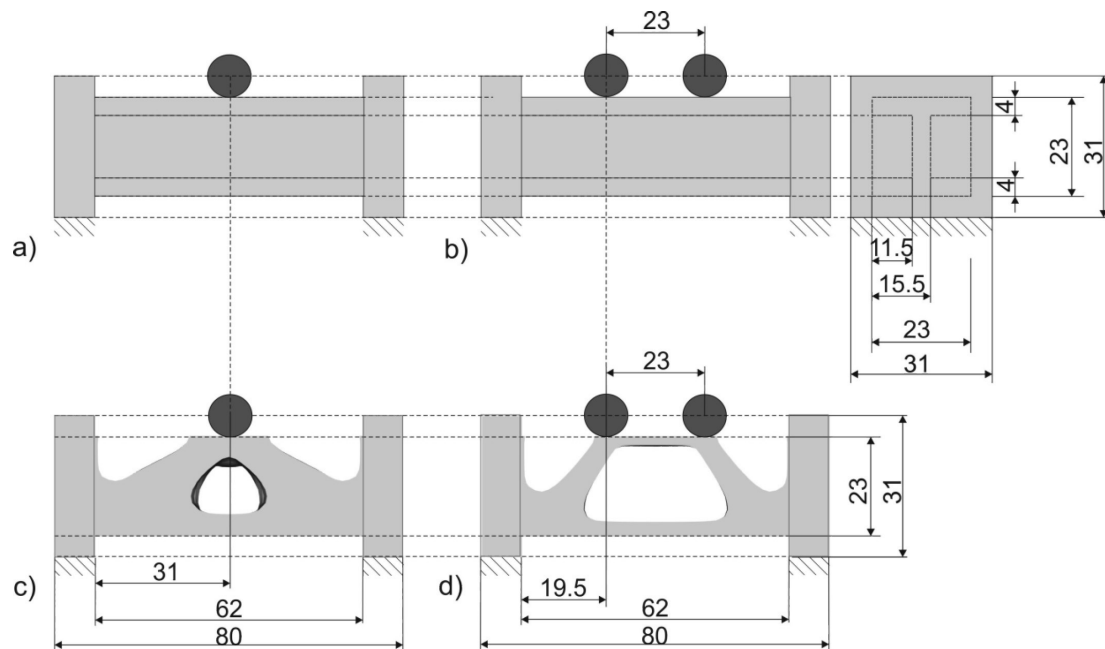


Figure 6. Representation of the sample geometry, the support surface and the position of the cylindrical support points via which the bending force was introduced into the sample; a) I-beam reference sample in a 3-point bending test, b) I-beam reference sample in a 4-point bending test, c) Topology-optimized sample in a 3-point bending test, and d) Topology-optimized sample in a 4-point bending test.

placed on a planar surface. In the three-point bending test, the force was applied selectively by means of a cylindrical support. Two cylindrical supports were used in the 4-point bending test. The I-beam specimens were tested under 3-point as well as under 4-point bending stress, analogous to the topology-optimized samples. All tests were carried out on the tensile-compression universal testing machine Z100 (Zwick Roell) analogous to the tensile tests presented previously. Due to the complex geometry, technical drawings are not shown and reference is made to the STL data in the appendix A.

4 Results and discussion

4.1 Materials properties of the investigated resin

The bending tests induce complex stress states in the structures: tensile stresses are present below the neutral fiber and compressive stresses above the neutral fiber in the I-beam. Furthermore, distinct shear stresses take place due to the ratio of length to height. Analogously to the stress distribution in an I-beam, tensile stresses are also acting at the bottom of the topology-optimized specimens. These

acting tensile forces are transmitted via cross struts between the two lower sample supports in both the 3- and the 4-point test samples. The more complex shape of the optimized structures amplifies the local presence of shear stresses, particularly at the intersection points of the individual trusses. Contrary to the pressure force transmission in an I-beam, the pressure force transmission inside the topology-optimized samples are in-line with the cross struts. From this consideration, it can be concluded that for the topology-optimized samples, the pressure forces are also transferred across the whole sample volume, which is not the case by the I-beam samples. Due to the different force transmission as a result of the varying sample geometry, the material properties were also determined by means of a tensile test depending on the direction of construction of the resin used.

If the tensile strength is the same in both the vertical and horizontal loading directions, the elongation at break of vertically loaded samples is more than half as small as in the horizontal loading direction. In addition, the material properties mentioned by the manufacturer in the "green" state could not be achieved either with regard to the material strength or the elongation at break. Researcher

were also unable to reproduce the manufacturer's material strength but concluded that the mechanical properties of the material are isotropic [14]. With this knowledge, the topology optimization is done with an isotropic material, but the topology-optimized samples were manufactured in such a way that the critical tension struts were set up horizontally with respect to the later acting tensile stresses (maximum strength and elongation at break).

However, most other additive manufacturing techniques besides stereolithography are known to produce anisotropic material properties: Structures produced with fused deposition modeling (FDM) inherent orthotropic properties depending on the print direction with the lowest stiffness and strength between layers [15, 16]. Regarding the additive manufacturing of metals, reports lower material properties of additively manufactured samples in the vertical loading direction compared to the horizontal loading direction [17]. For example, there are reports that the material properties of laser powder bed fusion processed 316L-steels specimens tested horizontally to the build-up direction are characterized by higher strengths and elongation values than specimens tested vertically to the build-up direction [18]. The reason for this can be attributed to the higher probability of a connection error between two successively compacted layers. The formation of connection errors in the laser powder bed fusion process can be attributed to an inhomogeneous or defective powder layer (9 inadequate fluidity of the powder, unsuitable particle size distribution) or due to inadequate sample com-

pression (flue gas formation and inadequate energy coupling, etc.). Applied to the topology-optimized structure, this means that the sample position and the associated direction of construction should take into account the later load during operation (here bending testing).

4.2 Defects density and morphology in stereolithography-processed bending samples

Defects varying in size and density could be recognized by the stereolithography-manufactured topology-optimized bending samples, *Figures 7, 8*. These defects were apparently on the sample surface. Statements regarding the defect morphology in the sample volume could be quantified in shape and size with the help of microtomography investigations. In order to make statements about the defect density and to map the effect of these defects on the component properties, all samples were examined before the mechanical test with regard to the defect size and the number of defects. Because of the size of the sample, a white distance between the x-ray source, sample and detector had to be maintained due to the geometry, so that the smallest resolving defect size is approximately $30\ \mu\text{m}$ to $40\ \mu\text{m}$. Statements on the effects of defects with a size smaller than $30\ \mu\text{m}$ to $40\ \mu\text{m}$ cannot be provided here due to the limited resolution.

Although all samples were produced with the same stereolithography system, the 4-point bending samples possess more defects than the 3-point bend-

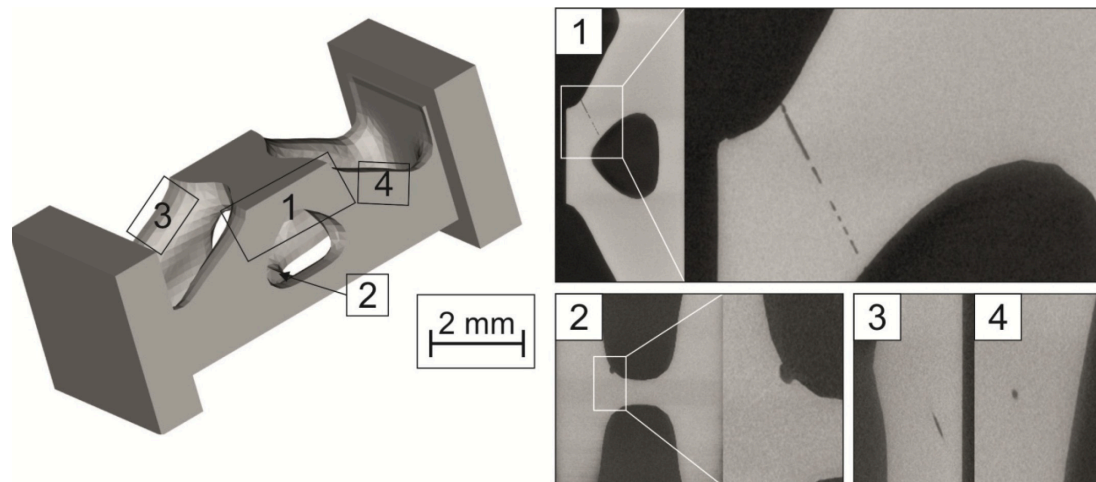


Figure 7. Defects within a 3-point test sample.

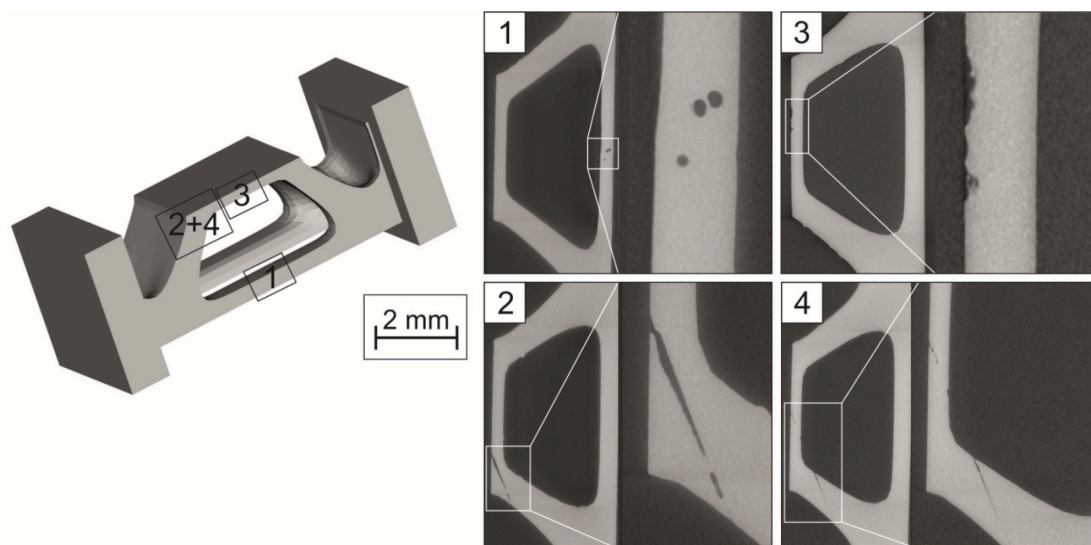


Figure 8. Defects within a 4-point test sample.

ing samples. While out of seven 3-point samples were free of defects, there was only one defect-free sample for the 4-point bending samples among the seven samples produced. The 3-point and 4-point bending samples were produced in two successive assembly jobs, whereby the 3-point bending samples were produced at first. It is assumed that the higher defect density in the 4-point bending samples is due to the fact that these were generated after the 3-point bending samples from the previously used resin, build platform and resin tank. Especially the transparent window at the bottom of the resin tank, through which the laser passes during the printing process, becomes locally “cloudy” with each layer printed impairing the print quality.

Three different types of defects can be detected in the stereolithography manufactured specimens. There are volume defects that have a spherical to channel-like structure, Figures 7, 8. The formation of the spherical defects can be attributed to the formation of gas pores that were formed or transported between the translucent vat bottom and the sample surface. In addition, channel-like defects can be observed, which are preferably formed at an angle of $20^\circ - 30^\circ$ at an angle to the building normal in the cross struts of the topology-optimized samples. During the formation of this defect, either there could have been a locally inadequate wetting of the sample surface with the resin, inhomogeneities within the bottom of the resin tank through which the polymerization laser passes, or a gas pore was

displaced laterally during the construction in the z direction as a result of the process sequence during the manufacturing process. In addition, near-surface defects can be registered, which increase the sample roughness, Figures 7, 8.

4.3 Mechanical properties of topology-optimized test specimens

The tolerable maximum bending force of the topology-optimized samples compared to the reference samples of the I-beam is shown in *Table 3*. The comparison of the average maximum force in the 3-point bending test between the I-beam sample (3-point) and the topology-optimized 3-point bending sample shows that the topology-optimized samples (defect free) on average endured an 8.36% higher force until failure occurred. A similar result can also be assigned to the comparison of the maximum tolerable load of the I-beam sample and the topology-optimized samples (defect free) in the 4-point bending test. The topology-optimized 4-point samples were able to bear a load that was 10.44% higher compared to the I-beam reference sample until failure took place.

For the 3-point bending tests the higher component stiffness of the topology-optimized samples can be seen from a higher slope in the course of the force-deflection curve compared to the I-beam reference samples, *Figure 9*. Another difference can

Table 2. Material properties determined in the tensile test for the used resin including the properties according to the manufacturer also given in Table 1.

Direction of loading	Tensile stress [MPa]	Elongation at break [%]
perpendicular	35.00 ± 1.58	3.88 ± 1.76
horizontal	35.00 ± 0.0	9.26 ± 1.09
manufacturer information	38–65	6.2–12

Table 3. Comparison of the measurement results from the 3-point and 4-point bending tests of the I-beam and the topology-optimized specimen.

Sample	I-beam, 3-point	I-beam, 4-point	optimized, 3-point	optimized, 4-point
load with defects [N]	3798 ± 108	4492 ± 103	4145 ± 193	5015 ± 535
load without defects [N]	3848 ± 90	4526 ± 67	4178 ± 173	5430 ± 286
reduction of load due to defects [%]	1.28	0.76	0.78	7.63
Increase of load due to topology optimization [%]	–	–	8.36	10.44

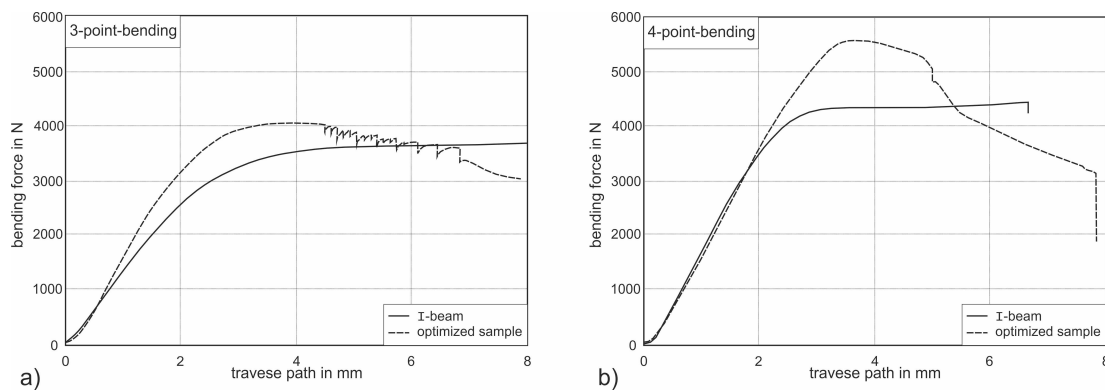


Figure 9. Representative force-compression diagram of the test specimens tested in a 3-point and 4-point bending test.

be seen from the higher tolerable loads of approximately 220 N of the topology-optimized samples in contrast to the reference I-beam specimens. However, the bending force of the topology-optimized samples drops in the direction of higher traverse path. Exceeding a traverse path of 4 mm to 5 mm, all force-compression diagrams show a jagged curve, which can be attributed to a partial failure of the samples. Catastrophic sample failure, characterized by a drastic drop in bending force, can only be registered if the traverse path is larger than 7 mm. In comparison, no catastrophic failure was observed in the I-beams. The abrupt failure of

the optimized structure can be explained by geometric aspects: the optimized structures are composed, primary by plate-like segments and some truss-like elements for the 3-point bending. The applied load is large enough to provoke finite deformations. Then, during increased loading, the structures start to strongly deform such severe stress rearrangements are present. For the large deformation and fractured state, of course, the optimization model cannot predict the correct solution since it is formulated for in terms of the linearized theory. Furthermore, for some prescribed deformation, the primary compression load states in the

plates exceeds a limit value and buckling initializes. This, of course, is accompanied by a sudden failure in stiffness contribution of the plates. Consequently, the entire structure fails in a catastrophic way. This gives rise to a future investigation when topology optimization for finite deformations is employed to answer the question whether optimization for the deformed state could prevent the sudden failure and additionally increase the structural stiffness further.

Although the I-beam samples took up a lower maximum bending force, they remained at a constant level in the crosshead travel considered up to 12 mm. For example, the I-beam sample only sagged due to the applied force, without failing. A similar behavior can also be assigned to the I-beam reference samples in the 4-point bending test. No catastrophic sample failure was observed in this test either. In comparison, catastrophic failure occurred in the topology-optimized samples, but with a higher bending force. The two curves also have a similar slope, so that the topology-optimized 4-point bending samples cannot be assigned a higher component stiffness compared to the I-beam reference samples, Figure 9b.

The topology-optimized samples were fragmented into small pieces in split seconds, preferably in struts, which are subjected to tension during bending testing, Figure 10. A rearrangement of the fractured pieces was not possible for most specimen. The course of the damage can also be described in such a way that the transverse struts on the underside of the specimen initially fail due to tensile stresses in the which failure was directly fol-

lowed by a failure of the cross struts as a result of the shear forces. Such a behavior indicates a more homogenous stress distribution and higher degree of material utilization: the optimized design has no unused structure features. This result is reasonable for homogenous minimization of the compliance energy over the whole body. However, such a high degree of material utilization results in fatal structure failure for the brittle material used here.

In addition, the influence of defects on the tolerable bending force was examined. To calculate the mean bending force (as load in N without defects), only the defect-free samples from the seven samples were taken into account, Table 2. The microtomography examinations carried out before the bending tests were used to identify the defect. The influence of the defects in the 3-point bending samples is small and the maximum tolerable bending force is reduced by only 0.76 % to 1.28 % in comparison to the defect-free mean force values. Another behavior can be assigned to the 4-point bending samples. Whereas the maximum bending force that can be achieved by the I-beam reference samples only drops by approximately 0.78 % in the 4-point bending test for the specimens with defects as compared to the mean values of the defect-free samples, the topology-optimized samples show a different behavior: here, the defects reduce the maximum bending force to be borne by 10.44 % compared to the defect-free reference samples. The higher drop in the maximum tolerable force due to the defects can be attributed to the much more complex geometry and the higher defect density (see section 4.2) in the 4-point bending test for the

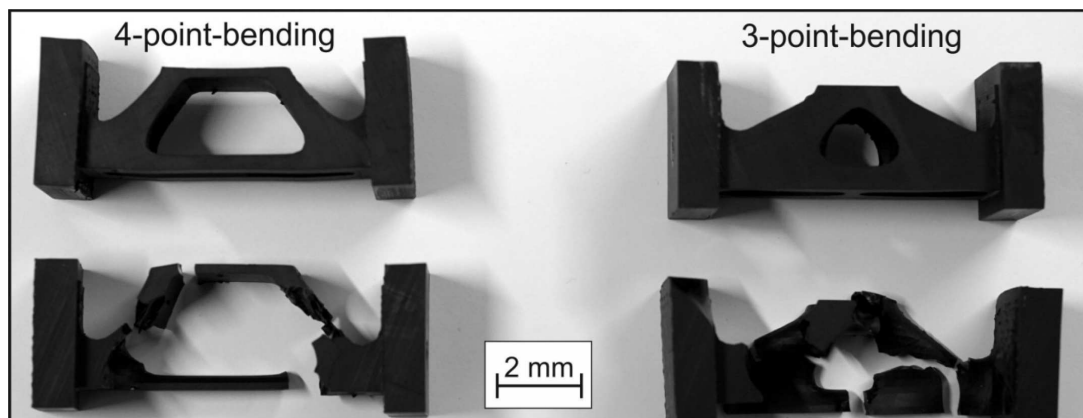


Figure 10. Comparison of selected samples before and after the bending test. The topology-optimized samples are characterized by catastrophic failure in the bending test with severe fragmentation.

topology-optimized samples. Without consideration of manufacturing defects, the topology optimization increases the maximum bearable forces by 8% to 10%, although no stress constraints or material failure is included in the optimization model with linear elastic material.

5 Conclusions and outlook

In this work, we examined the effect of topology optimization based on strain energy minimization (compliance minimization) that undergo bending loading in 3- and 4-point test devices. The following statements can be made:

- By optimizing the topology regarding the strain energy without additional stress constraints, the tolerable maximum forces in the 3-point bending test could be increased by 8.36% and in the 4-point bending test by 10.44% as compared to the reference samples of simple I-beams.
- The increase of structural stiffness, i.e. the force-displacement response at the loading point, was less prominent in the 3-point bending example and nearly negligible for the 4-point bending.
- Microtomography examinations confirm the presence of defects on the component surface and in the component volume.
- The defects reduce the maximum tolerable bending forces and lead to premature sample failure.
- The failure of the topology-optimized samples was characterized by severe fragmentation indicating a more homogenous stress distribution within the structure.

Although a linear elastic material with compliance minimization optimization and no constraints for maximum stress were considered, experiments with additively manufactured specimens showed significantly increased strength, although only minor improvement in structural stiffness, i.e. force-displacement response. The structural stiffness could only be increased for the 3-point bending compared to the reference design (I-beam). The negligible improvement in structural stiffness for the 4-point bending could result from the I-beam beam being already nearly optimal for this case. However, the compliance minimization optimization actually minimizes the strain energy of the whole body, not only the force-displacement response at the loading point. The characteristics of

the homogenous optimization regarding the minimization of the strain energy over the whole structure is therefore clearly noticeable in the experimental results: the structural stiffness is increased slightly, but the stress is distributed more equally throughout the structure resulting in the characteristic failure of the structures, i.e. severe fragmentation at higher maximum forces.

Material defects and other production pending effects were analyzed and their influence was minimized for the final results. An over-all increased performance of basic structures over standard geometries (i.e. I-beam) could be performed by applying a topology optimization for linear elastic material without specific manufacturing constraints and production via prosumer level additive manufacturing-equipment.

The material produced with stereolithography was assumed to be isotropic regarding the optimization. Anisotropic structures resulting from most other additive manufacturing techniques could be modeled with the thermodynamic optimization [11]. Future research could also consider special cases of anisotropy, i.e. an optimization of the print plane and direction. Optimization with regard to material defects and/or uncertainty would improve the results in situ, which would require a more sophisticated optimization model as well as further experimental investigations on the specific additive manufacturing process itself.

Acknowledgement

We thank Ms. Claudia Brügge and Mr. Christian Schollmeier for carrying out the mechanical tests. Open access funding enabled and organized by Projekt DEAL.

6 References

- [1] G. Rozvany, *Struct. Multidiscip. Optim.* **2009**, 37, 217.
- [2] O. Sigmund, K. Maute, *Struct. Multidiscip. Optim.* **2013**, 48, 1031.
- [3] J.D. Deaton, R.V. Grandhi, *Struct. Multidiscip. Optim.* **2014**, 49, 1.

- [4] S.H. Huang, P. Liu, A. Mokasdar, L. Hou, *Int. J. Adv. Manuf. Technol.* **2013**, *67*, 1191.
- [5] W. Gao, Y. Zhang, D. Ramanujan, K. Ramani, Y. Chen, C.B. Williams, C.C. Wang, Y.C. Shin, S. Zhang, P.D. Zavattieri, *Comput. Aided Des.* **2015**, *69*, 65.
- [6] H. Bikas, P. Stavropoulos, G. Chryssolouris, *Int. J. Adv. Manuf. Technol.* **2016**, *83*, 389.
- [7] D. Brackett, I. Ashcroft, R. Hague, Proceedings of the solid freeform fabrication symposium, Austin, TX Bd. **2011**, *1*, 348.
- [8] T. Zegard, G.H. Paulino, *Struct. Multidiscip. Optim.* **2016**, *53*, 175.
- [9] J. Liu, A.T. Gaynor, S. Chen, Z. Kang, K. Suresh, A. Takezawa, L. Li, J. Kato, J. Tang, C.C. Wang, *Struct. Multidiscip. Optim.* **2018**, *57*, 2457.
- [10] D.R. Jantos, K. Hackl, P. Junker, *Int. J. Numer. Methods. Eng.* **2019**, *117*, 991.
- [11] D.R. Jantos, K. Hackl, P. Junker, *Struct. Multidiscip. Optim.* **2020**, *61*, 2135.
- [12] G. Gaganelis, D.R. Jantos, P. Mark, P. Junker, *Struct. Multidiscip. Optim.* **2019**, *59*, 2227.
- [13] M.P. Bendsøe, O. Sigmund, *Arch. Appl. Mech.* **1999**, *69*, 635.
- [14] F. Cosmi, A. Dal Maso, *Mater. Today: Proc.* **2020**.
- [15] S. Ahn, M. Montero, D. Odell, S. Roundy, P.K. Wright, *Rapid Prototype. J.* **2002**.
- [16] A. Bellini, S. Güceri, *Rapid Prototype. J.* **2003**.
- [17] D. Herzog, V. Seyda, E. Wycisk, C. Emmelmann, *Acta Mater.* **2016**, *117*, 371.
- [18] A. Röttger, J. Boes, W. Theisen, M. Thiele, C. Esen, A. Edelmann, R. Hellmann, *Int. J. Adv. Manuf. Technol.* **2020**, *1*.

Received in final form: June 27th 2022